ChemPhysChem

Research Article
doi.org/10.1002/cphc.202400050

Chemistry Europe
European Chemical Societies Publishing

www.chemphyschem.org

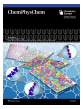

Simple Method to Assess Foam Structure and Stability using Hydrophobin and BSA as Model Systems

Judith Krom,*[a] Konrad Meister,[a, b] and Thomas A. Vilgis*[a]

The properties and arrangement of surface-active molecules at air-water interfaces influence foam stability and bubble shape. Such multiscale-relationships necessitate a well-conducted analysis of mesoscopic foam properties. We introduce a novel automated and precise method to characterize bubble growth, size distribution and shape based on image analysis and using the machine learning algorithm *Cellpose*. Studying the temporal evolution of bubble size and shape facilitates conclusions on foam stability. The addition of two sets of masks, for tiny bubbles and large bubbles, provides for a high precision of analysis. A python script for analysis of the evolution of bubble diameter, circularity and dispersity is provided in the Supporting Information. Using foams stabilized by bovine serum albumin (BSA), hydrophobin (HP), and blends thereof, we show how this technique can be used to precisely characterize foam structures. Foams stabilized by HP show a significantly increased foam stability and rounder bubble shape than BSA-stabilized foams. These differences are induced by the different molecular structure of the two proteins. Our study shows that the proposed method provides an efficient way to analyze relevant foam properties in detail and at low cost, with higher precision than conventional methods of image analysis.

Introduction

Protein-stabilized foams are ubiquitous in everyday life - from milk foam in a morning cappuccino to whipped cream on an afternoon cake to beer foam in the evening. The macroscopic appearance of foams is determined by their complex microstructure. Therefore, reliable characterization of the microstructure of different foams is a fundamental requirement for understanding how molecular differences influence foam stability and coarseness.

To characterize foam stability, traditionally the foam volume at two different points in time is measured and the foam stability is calculated by $FS = V_t/V_0$, where V_t is the foam volume at the later point in time and V_0 is the initial foam volume.[1–7] Commercially available foam analyzing instruments additionally allow for analysis of bubble size.[8] However, these instruments are quite cost-intensive and not readily available in most labs. In contrast, the method developed in the following can be applied to images taken with a common optical microscope and freely available open-source software.

Image analysis of microscope images is a powerful tool that allows for a quantitative analysis of microstructures.[9–11] To determine the sizes of objects, such as bubbles in a foam, cells in biological systems or ice crystals, diameters of these objects can be measured manually using programs such as *Fiji/ImageJ*.[12–14] This is easy to perform and does not require special programming skills or financial investment in expensive instruments. However, for large numbers of objects it can become extremely time intensive. Therefore, a common method is to just measure the ten largest objects with the drawback that precision is compromised.[13]

Another method is, to set a threshold and convert the image into a binary image. From the connected same contrast pixels, objects can then be identified.[15–18] However, for objects, which are not sufficiently separated from each other, whose intensity profiles do not decay smoothly from the center, or if the center of the object has the same color as the background, the correct identification of the objects by this method is difficult.[19]

Foams consist of air bubbles dispersed in a liquid, which are stabilized by emulsifiers (surfactants, proteins). The thin liquid films between bubbles are referred to as lamellae.[20,21] Wet foams, which contain a higher liquid fraction, show larger areas of liquid in between the bubbles. In a microscope image, such parts of the continuous (liquid) phase have the same contrast as the bubble interior. Therefore, methods of image analysis, which are based only on a threshold are not sufficient to adequately determine the bubble areas.

To provide additional criteria for segmentation and analyze microscope images in an automated way, deep neural network-based methods are frequently applied in the fields of cell biology and biomedical applications.[19,22–31] These usually require large training datasets to estimate the parameters for

[a] J. Krom, K. Meister, T. A. Vilgis
Max Planck Institute for Polymer Research,
Ackermannweg 10, 55128 Mainz, Germany
E-mail: kromj@mpip-mainz.mpg.de
meisterk@mpip-mainz.mpg.de
vilgis@mpip-mainz.mpg.de

[b] K. Meister
Department of Chemistry and Biochemistry,
Boise State University,
Boise, Idaho 83725, United States

Supporting information for this article is available on the WWW under https://doi.org/10.1002/cphc.202400050

segmentation. Mostly, such models are trained on specialized datasets and come with the drawback of not generalizing well to other types of data.[19] Thus, Stringer et al. used a variety of different training data in the process of developing the open-source software *Cellpose*:[19] large datasets of cell images obtained from different types of microscopy and using a variety of fluorescent markers were collected and manually segmented, as well as non-microscopy images containing large numbers of repeated objects.

By including such data in the training set a neural network was trained that generalizes more robustly and more widely. When analyzing an image in *Cellpose*, the neural network predicts horizontal and vertical contrast gradients and whether a pixel belongs to any cell. These maps are then combined into a gradient vector field, which is used to assign the pixels to their eventual fixed point. All pixels converging to the same fixed point are then assigned to the same mask. This approach provided *Cellpose* a high precision compared to other segmentation algorithms,[19] and avoids the above-mentioned disadvantages of an exclusively contrast-based segmentation.

When applying software developed for segmenting cells to foams, a challenge is the heterogeneous nature of foams. Since cells of one tissue have a rather homogeneous size, segmentation software programs can have difficulties to detect very small and very large objects at the same time. However, due to Ostwald-ripening, foams offer a very broad size distribution. Therefore, adequate analysis necessitates a procedure that can detect tiny as well as large bubbles. Indeed, when reviewing different methods of foam analysis, it becomes apparent, that tiny bubbles are often not considered and their relevance is not discussed.[17,32]

In the current article, a method is presented to precisely analyze the temporal evolution of bubble shape and size over the whole range of bubble sizes. Our considerations are based on a script we wrote in the programming language *Python* to analyze microscope images of liquid foams. We provide this script in the Supporting Information accompanying this manuscript. For pre-processing of the microscope images, we follow similar steps as described by Bonilla et al., who used *ImageJ*.[32] The images are then analyzed using *Cellpose*[11,19]. *Cellpose* offers several pretrained models and can be further trained on own data.[11] Additionally, it offers the possibility for manual corrections of bubble masks via a graphical user interface (GUI).

In contrast to Bonilla et al.[32] or Saad et al.,[13] we here implement a method to overcome the shortcomings of *Cellpose* in terms of size range. Therefore, to improve the precision of the method we append the possibility to merge two sets of masks for each image to cover a larger size distribution. This is unique and offers a higher precision in detecting the whole bubble size range. Furthermore, we remove bubbles at the edge of the microscope image, which are not shown completely. Removal of such edge bubbles adds to the precision of analyzing the shape and correct size of the investigated bubbles. The use of a machine learning algorithm and the supplied script provide for a faster and more detailed analysis than with conventional methods. Therefore, the presented approach offers a fast and easy analysis of a large amount of bubbles.

Furthermore, in contrast to Bonilla et al.,[32] we consider a time series of microscope images to quantify foam stability. The evolution of bubble sizes over time correlates with the stability of a foam, since the mean bubble size increases with time due to coalescence and Ostwald ripening.[20,33,34] The bursting of bubbles and the escape of air from the foam leads to a macroscopically observed foam decay.

To monitor the mean bubble size, we use the equivalent bubble diameter, which is the diameter of a sphere with the same area as the bubble. Furthermore, we characterize the bubble size distribution by analyzing the dispersity of the bubble sizes (areas). In addition, the bubble shape is considered by analyzing the circularity of the bubbles in the foam. By these means, we offer a method to quantify foam structure and stability simultaneously.

Two model foams with different bubble characteristics, stabilized by two proteins with different structures, bovine serum albumin (BSA) and hydrophobin (HP), are considered to illustrate how the method works. Due to their characteristic primary and secondary structure, the proteins show different arrangements at air-water interfaces, leading to very distinguishable foam structures. Consequently, it is useful to consider mixtures of these proteins to test the method.

BSA is a "heart-shaped" protein with a molecular weight of about 66.5 kDa.[35–37] It contains 583 amino acids (607 amino acids including the signal peptide)[38] and is found in the blood serum of bovines and cow's milk.[39–41] HP on the other hand is a small protein with a molecular weight of about 10 kDa[42] and a primary structure containing about 100 amino acids.[43,44]

HPs are secreted by filamentous fungi and have multiple biological functions.[42,43,45–47] This protein family is divided into two classes, class I and class II hydrophobins. Representatives of these two classes differ in their spacing between cysteine residues, which are generally longer and vary more for class I HPs.[48,49] Furthermore, class I and class II HPs differ in their solubility, the location of hydrophobic patches at the protein surface, and the structures they form upon assembly at hydrophilic : hydrophobic interfaces.[46,50] In the current study a class I hydrophobin is used.

Furthermore, HPs are highly surface-active proteins due to their almost janus-like amphipathic nature[51] and their rigidity.[52] HPs contain 4 disulphide bonds which stabilize the core.[44] The high core stability ensures the exposition of a large hydrophobic patch to the protein surface,[44,53] which provides HPs with surfactant like characteristics.[45,54] At a hydrophilic: hydrophobic interface, HPs spontaneously self-assemble into an amphipathic protein layer.[44] Due to their properties, HPs lower the surface tension significantly[44,47,55,56] and the HP layers at the air-water interface show a high elasticity.[51] They are known to form some of the most stable aqueous foams.[45,57–59]

The tertiary structures of BSA and HP are shown in Figure 1 to illustrate their fundamental differences in shape and primary structure, which determine their surface activity and cause distinct variations in bubble shape, size distribution, and growth rate after foam preparation.

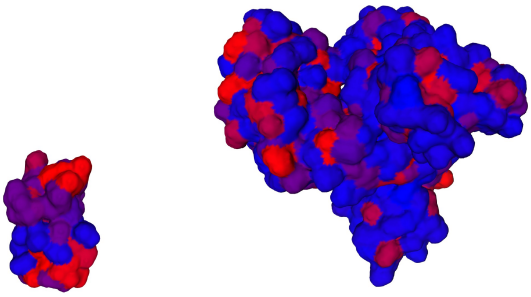

Figure 1. Surfaces of the protein structures of (a) HP (UP-ID: P16933, containing 136 amino acids) and (b) BSA (UP-ID: P02769, containing 583 amino acids). Hydrophobic amino acids are colored in red and hydrophilic ones in blue.[38]

Materials and Methods

Sample Preparation

BSA (A7030, heat shock fraction, protease free, fatty acid free, essentially globulin free, pH 7, ≥98%) from Sigma–Aldrich (Saint Louis, MO, USA) and HP (H*B hydrophobin) from BASF (Ludwigshafen, Germany) were used as-received. To ensure complete dissolution, HP solutions were stirred for 48 h (cf. Ref. [48,60]). Solutions of 4 wt% protein in ultrapure water (18.2 MΩcm) were prepared. This protein concentration was chosen, because whipping requires a protein concentration of 3% to 40%[61] and because it resulted in smooth foams.

Foam Formation

For foam formation a T 25 easy clean control ULTRA TURRAX (IKA-Werke GmbH & Co. KG, Staufen, Germany) equipped with dispersion tool S 25N-10G was used. 2 g of protein solution were dispersed at a speed of 20000 rpm for 1 min. The glass vessel used for foaming the protein solution was a custom-built glass cylinder with overflow protection in the upper part. The inner diameter of the glass cylinder was 13.6 mm, the height of the cylinder without overflow protection was 65 mm and the total height of the glass vessel was 90 mm. An image of the glass vessel is shown in Figure 2. The larger diameter in the upper part prevents overflowing of the foam (overflow protection).

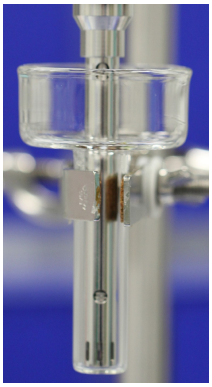

Figure 2. Glass vessel used for foam formation with ultra turrax tool inserted. The upper part with larger diameter prevents the foam from overflowing during ultra turrax treatment.

Optical Microscopy

Immediately after preparation, 0.01 g of foam were transferred to a microscope slide using a microspoon and then covered with a cover slip. Three little pieces of teflon film with a thickness of 50 µm served as spacer between microscope slide and cover slip. Bright field optical microscopy with 1.6-fold magnification was performed in transmission mode using a Leica MS5 stereomicroscope (Leica Microsystems GmbH, Wetzlar, Germany). Microscope images were taken every 5 min for 30 min. Microscopy was performed for three identical samples.

Image Analysis

Data was analyzed using a Fujitsu (Minato, Tokyo, Japan) Esprimo P757 computer with Intel®Core™i7-6700 CPU @ 3.40 GHz, 3408 MHz, 4 cores, 8 logical processors and 16.0 GB of RAM operating in Microsoft (Redmond, WA, USA) Windows 10 Pro.

For image analysis *Cellpose*[11,19] and *Python* (Python Software Foundation, version 3.8.8) were used.

Pre-processing was performed in *Python* applying gaussian blur filter (cv2.GaussianBlur), image subtraction (cv2.subtract (2 times)), kuwahara filter (pykuwahara 0.3.2), background subtraction (skimage.restoration.rolling_ball, skimage.restoration.ellipsoid_kernel) and contrast enhancement (PIL.ImageEnhance.Contrast) to the original images.

Cellpose was trained on microscope images using the GUI. The predefined model "CP" was taken as starting point and was adjusted by training on one own image to adjust for tiny bubbles and another own image to adjust for large bubbles. To identify the foam bubbles, the images were processed in the *Cellpose* GUI with the trained model. Slight corrections to bubble masks have been made in individual cases. *Cellpose* provides a "_seg.npy"-file, which contains an array of the bubble masks. In this array, each pixel of the image is labelled with a number. The background is labelled with 0 and all masks are labelled with ascending integers.

Further analysis was performed in *Python* to add masks of small and large bubbles, remove edge bubbles and analyze bubble properties. To obtain the equivalent diameter, the area, and the crofton perimeter of each mask, we used the package skimage.measure.regionprops_table. The mean equivalent bubble diameter of all bubbles in an image, the mean circularity, and the dispersity were calculated from these data. When calculating the mean circularity, only circularities of bubbles with an equivalent diameter larger than 10 pixels were considered to minimize uncertainties caused by image resolution. Mean and standard deviations of measurements of three identical samples were calculated. For each quantity the time-dependent cause was evaluated.

Results and Discussion

Image Processing and Analysis

Figure 3 shows the workflow of the image analysis. An optical microscope image is shown in Subfigure a (upper left). The edges of the bubbles are darker, however, the insides of the bubbles have the same contrast as the lamellae. Subfigure b (upper right) displays the pre-processed image. A gaussian blur filter, image subtraction and kuwahara filter are applied to reduce image noise. Subsequently, the background subtraction

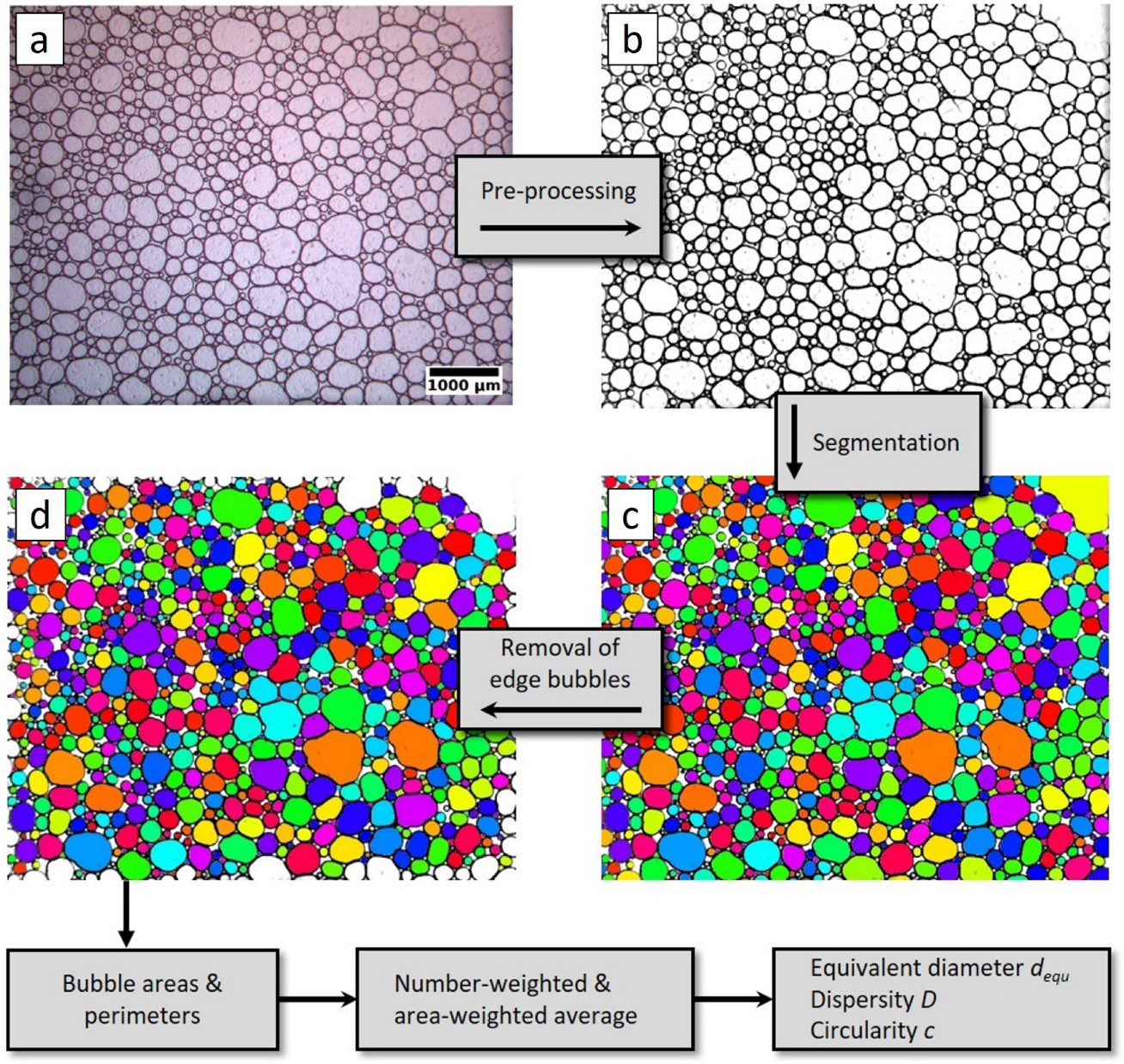

Figure 3. Image processing: The original microscope image is pre-processed to reduce background noise and enhance contrast. Bubble masks are detected using *Cellpose* (Segmentation). Subsequently, masks of edge bubbles are removed. From the remaining masks bubble areas and perimeters are determined, averages are calculated and the mean equivalent diameter, mean circularity and dispersity are calculated for each image.

is used to smooth the background. Finally, the contrast of the image is enhanced. All preprocessing steps are performed using *Python*.

After image pre-processing, *Cellpose* is used to identify the bubbles, as shown in Subfigure c (lower right). The contrast of the edges is used to identify the bubbles. In the segmentation, the bubbles become individual masks and are colored randomly to improve the discriminability. An array containing all bubble masks is saved. The quantification and evaluation of the bubbles is done in *Python*. If there is a very heterogeneous size distribution of the bubbles, *Cellpose* is not able to detect all bubbles in an image. Our *Python* script allows to add two sets of masks (one for small bubbles and one for large bubbles) to solve this problem and to identify bubbles in a larger size range.

In our *Python* code, edge bubbles are neglected. The image in Subfigure d (lower left) shows the remaining bubble masks in different colors. These are overlaid with the preprocessed microscope image so that removed bubbles are shown in white. If only a small part of a bubble is visible in the image, treating that part as a whole bubble can distort the statistical analysis, especially in the case of large bubbles. To remove edge bubbles the criterion:

$$I = \begin{cases} < \frac{1}{4} d_{equ} \Rightarrow \text{consider bubble} \\ > \frac{1}{4} d_{equ} \Rightarrow \text{do not consider bubble} \end{cases} \quad (1)$$

is applied, where I is the length (number of pixels) the bubble shares with the edge of the image and d_{equ} the equivalent diameter of the bubble. Figure 4 illustrates this approach.

Cellpose provides an array with bubble masks, that can be analyzed in *Python*. The bubble areas, equivalent diameters, and perimeters (in pixels) for all detected masks can be obtained using the scikit-image library. The equivalent diameter is the diameter of a circle with the same area as the bubble, as noted in Eq. (2):

$$d_{equ} = \sqrt{\frac{4}{\pi} A} \quad (2)$$

where A is the actual bubble area in the microscope image. For each image, we calculate the mean equivalent bubble diameter of all bubbles in the image.

To characterize the shape of the bubbles, the circularity of each bubble is calculated as:

$$c = \frac{4\pi A}{p^2} \quad (3)$$

where A is the area of the bubble and p is the perimeter. The circularity is 1.0 for a perfect circle and as it approaches 0.0, it indicates an increasingly elongated shape. Subsequently, the mean circularity of all bubbles in one image is calculated.

The characterization of the bubble size distribution in an image is done by calculation of the dispersity. Analogously to polymer chemistry, where the dispersity of molar masses is given by:[62,63]

$$D = \frac{\overline{M}_\omega}{\overline{M}_n} \quad (4)$$

with M_ω mass weighted average of the molar mass and M_n number weighted average of the molar mass, we define the bubble dispersity:

$$D := \frac{\overline{A}_\alpha}{\overline{A}_n} \quad (5)$$

where $\overline{A}_\alpha$ is the area weighted average of the bubble areas and $\overline{A}_n$ is the number weighted average (=mean) of the bubble areas.

Optical Microscopy of HP- and BSA-Stabilized Foams

Figure 5 shows pre-processed optical microscope images of HP- and BSA-stabilized foams at different time steps. Clear differences in the temporal behavior can be distinguished between foams only containing HP and those only containing BSA. The bubble shape, size distribution and growth rate vary significantly between these foams. A visual comparison of the microscope images of these two different foams (first and last row in Figure 5) shows that the bubbles in the BSA-stabilized foam have a broader size distribution and their increase in size is more pronounced. Over time, the bubble shape changes from spherical to polyhedral. The bubbles in the HP-stabilized foam not only have a narrower size distribution and remain smaller over time, but also have a different shape. Although the HP-stabilized foam bubbles become less spherical over time, the vertices remain rounded.

Additionally, Figure 5 also shows microscope images of foams stabilized by blends of HP and BSA (rows two through

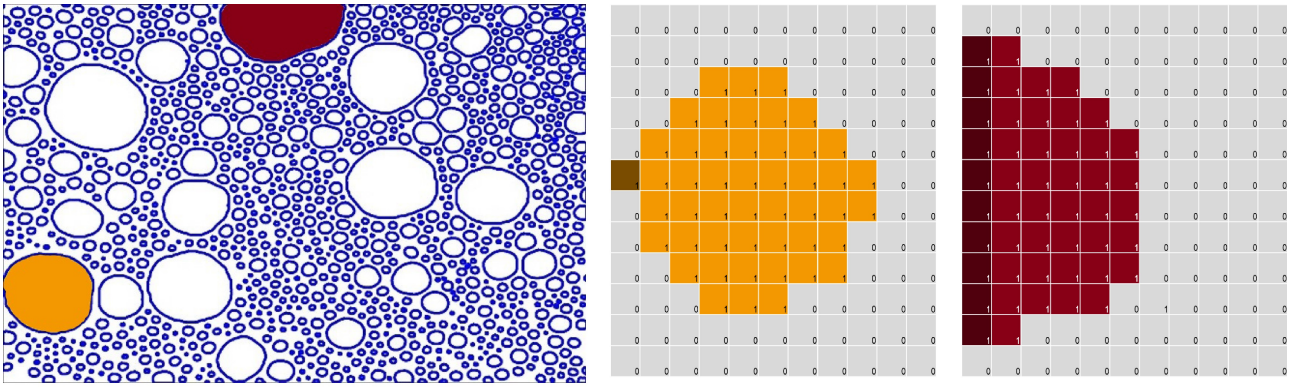

(a) Outlines of all detected bubble masks are shown in blue. Bubbles like the orange one should be evaluated, bubbles like the red one should not be considered.

(b) $A = 48$
$d_{equ} = 8$
$l = 1$
$\Rightarrow l < \frac{1}{4} d_{equ}$
$\Rightarrow$ Bubble will be evaluated.

(c) $A = 48$
$d_{equ} = 8$
$l = 10$
$\Rightarrow l > \frac{1}{4} d_{equ}$
$\Rightarrow$ Bubble will be removed.

Figure 4. Illustration of the removal of edge bubbles. Edge bubbles with $l > \frac{1}{4} d_{equ}$ are removed. l is the length the bubble shares with the image edge, d_{equ} is the equivalent diameter of the bubble calculated from its area.

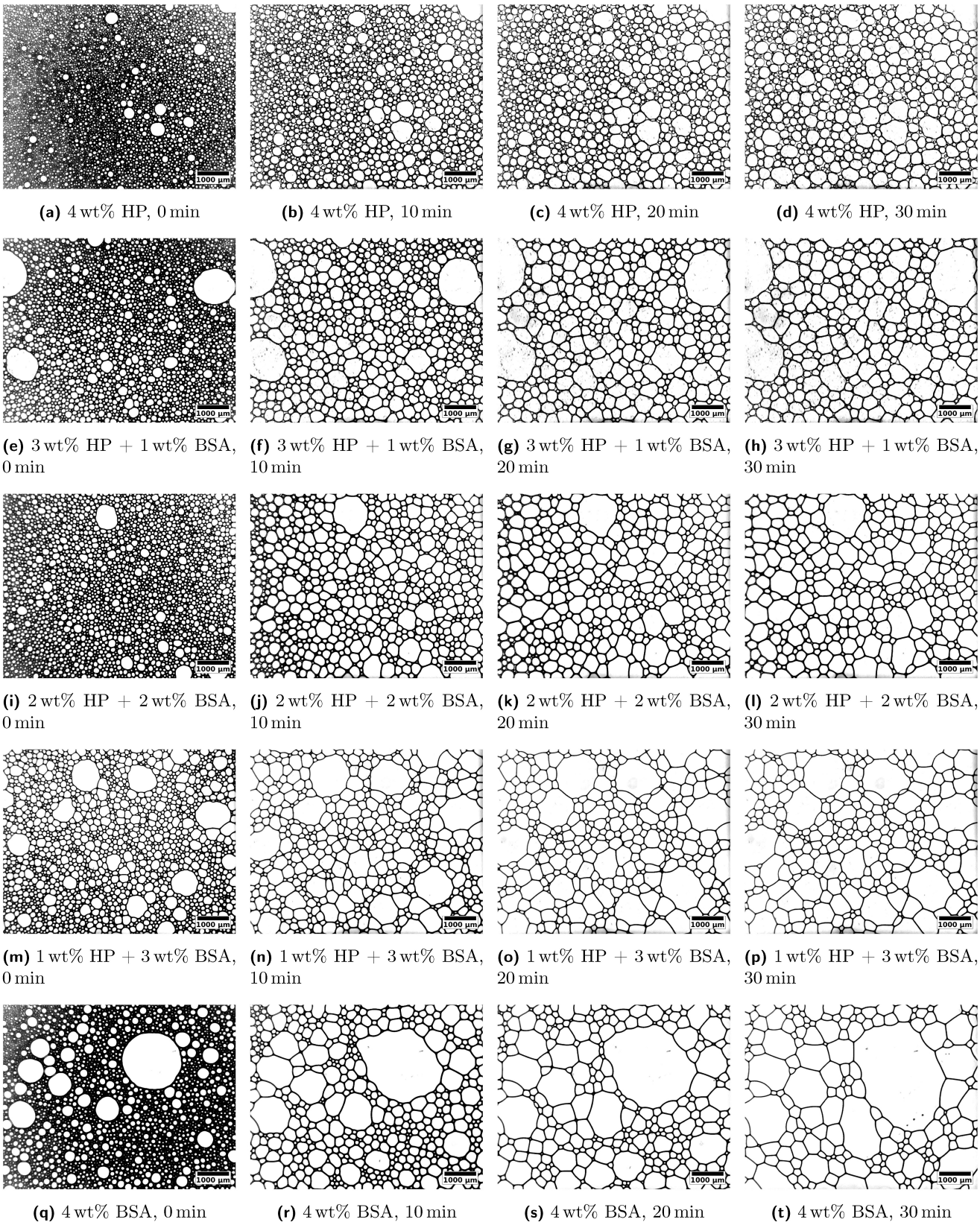

(a) 4 wt% HP, 0 min **(b)** 4 wt% HP, 10 min **(c)** 4 wt% HP, 20 min **(d)** 4 wt% HP, 30 min

(e) 3 wt% HP + 1 wt% BSA, 0 min **(f)** 3 wt% HP + 1 wt% BSA, 10 min **(g)** 3 wt% HP + 1 wt% BSA, 20 min **(h)** 3 wt% HP + 1 wt% BSA, 30 min

(i) 2 wt% HP + 2 wt% BSA, 0 min **(j)** 2 wt% HP + 2 wt% BSA, 10 min **(k)** 2 wt% HP + 2 wt% BSA, 20 min **(l)** 2 wt% HP + 2 wt% BSA, 30 min

(m) 1 wt% HP + 3 wt% BSA, 0 min **(n)** 1 wt% HP + 3 wt% BSA, 10 min **(o)** 1 wt% HP + 3 wt% BSA, 20 min **(p)** 1 wt% HP + 3 wt% BSA, 30 min

(q) 4 wt% BSA, 0 min **(r)** 4 wt% BSA, 10 min **(s)** 4 wt% BSA, 20 min **(t)** 4 wt% BSA, 30 min

Figure 5. Microscope images of foams stabilized by HP (first row), HP-BSA mixtures (second to forth row), and BSA (last row). Time proceeds from left to right.

four). Three different ratios of HP to BSA were considered (3:1, 2:2, and 1:3). The foams stabilized by mixtures of HP and BSA are less stable than foams stabilized by HP alone, but more stable than foams stabilized by BSA, since the bubble sizes

grow faster than for HP- but slower than for BSA-stabilized foams. BSA-stabilized foams have the widest bubble size distribution. The bubble shapes of foams stabilized with blends of HP and BSA look more like the purely BSA-stabilized foams. To quantify these visually observed differences, the temporal evolution of the mean equivalent bubble diameter was analyzed and the dispersity and mean circularity of the bubbles were calculated.

Temporal Evolution of Mean Bubble Size

As foams age, the mean bubble size increases due to coalescence and Ostwald ripening.[20,33,34] As the bubbles grow and burst, the foam decays. Therefore, the mean bubble size over time is a measure of foam stability. Figure 6 shows the mean equivalent bubble diameter over time for HP- and BSA-stabilized foams. Throughout the measurement period, the mean bubble size of HP-stabilized foams remains significantly smaller than that of BSA-stabilized foams. Proteins can adsorb at an air-water interface due to hydrophobic amino acid residues.[64] As with most proteins, the majority of the surface amino acid residues of BSA are hydrophilic.[38,64]

However, BSA also has some hydrophobic amino acids on its surface that allow it to attach to the bubble surfaces and thus stabilize the foam. HP has a different molecular structure with a large hydrophobic part on its surface, which makes it a very surface-active molecule.[44,64] At air-water interfaces, HP molecules pack very tightly and form very strong films that can significantly resist bubble shrinkage.[64]

Class I hydrophobins form insoluble rodlet films at air-water interfaces when the surface membrane gets compressed.[45] Since foams are dynamic systems where bubbles shrink and others grow at their expense (Ostwald ripening),[59,65,66] the HP films at the interface are not static either. The HPs at the surface of a shrinking bubble experience compression and can therefore form rodlet structures. These very stable films around the small bubbles prevent further shrinkage. As a result, larger bubbles cannot grow at their expense and the foam becomes more stable as observed by optical microscopy.

In addition, HP has a lower molecular weight than BSA. Therefore, it can move faster to the interface, assemble at the interface while the bubbles are still small, and stabilize the bubbles in the liquid. By forming stable HP films, the bubbles stay smaller. Furthermore, HP has the ability to significantly lower the surface tension and achieves lower surface tensions than BSA.[44,56] A lower surface tension allows for a larger surface area. The surface of more smaller bubbles adds up to a larger area than a smaller number of larger bubbles filled with the same total volume of air. The lower surface tension caused by HP favors the many small bubbles observed in HP-stabilized foams.

Temporal Evolution of Circularity

As discussed in the literature, foams dry during aging and the bubble shape changes from spherical to polyhedral.[67–69] These changes in bubble shape can also be seen in the microscope images in Figure 5. When looking at the microscope images, it is noticeable that the bubble shape varies between HP-stabilized and BSA-stabilized foams. BSA-stabilized foams form polygonal shapes as they age. Although the overall shape of the bubbles in HP-stabilized foams is similar to polygonal, the vertices are rounded.

Circularity compares the area of the bubble to the area that a circle with the perimeter of the bubble would have, and is therefore a measure of how close the shape of the bubble under consideration is to that of a perfect circle. We use circularity to compare the bubble shapes of BSA-stabilized and HP-stabilized foams. Figure 6 shows the temporal evolution of the bubble circularity of HP- and BSA-stabilized foams. Over time, the circularity of the bubbles decreases as the bubble shape changes from circular to polygonal. This decrease in circularity with time is observed for both systems. At $t = 0$, both, HP- and BSA-stabilized foams show a mean circularity close to 1. This means that the bubbles are spherical, which is consistent with what can be observed in the microscope images. However, at all later time steps, the circularity of the HP-stabilized foams is significantly higher than that of the BSA-stabilized foams, which means that the bubbles in the HP-stabilized foams have a rounder shape (their shape is closer to a circle). The bubbles in the HP-stabilized foams are less elongated than some bubbles in the microscope images of the BSA-stabilized foams. In addition, the vertices of the bubbles in the HP-stabilized

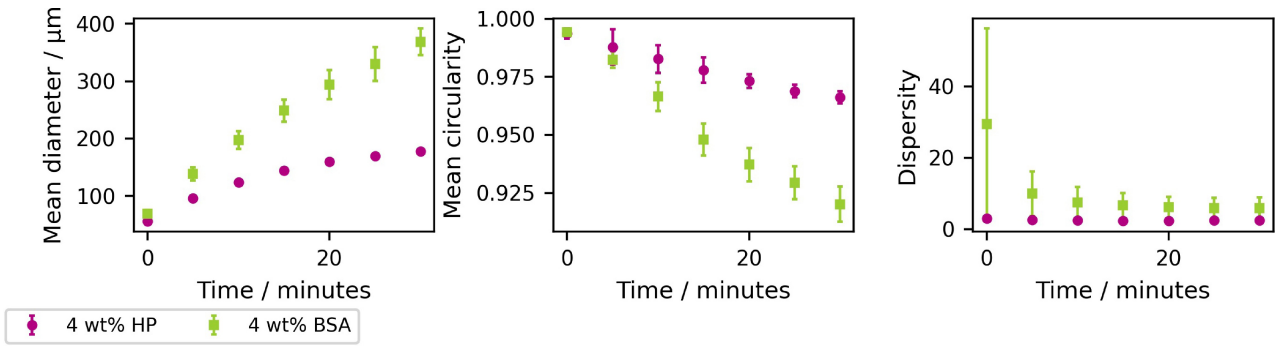

Figure 6. Comparison of the temporal evolution of mean equivalent bubble diameter, mean circularity and dispersity of HP- and BSA-stabilized foams.

foams are rounded. Both of these effects cause the higher circularity observed in the HP-stabilized foams.

Temporal Evolution of Dispersity

To quantify the variation in bubble size within an image, we calculated the dispersity of the bubble size. The temporal behavior of the dispersity of HP- and BSA-stabilized foams is shown in Figure 6. Especially in the beginning there are many small bubbles and few large bubbles. Therefore, a higher dispersity is observed (especially for BSA-stabilized foams). Over time, Ostwald ripening and coalescence cause small bubbles to disappear. Therefore, the distribution of bubble sizes shifts and the dispersity decreases.

HP-stabilized foams show a more homogeneous bubble size distribution and smaller dispersity than BSA-stabilized foams. This result is consistent with the visually observed foam properties in the microscope images. The narrower size distribution observed for HP-stabilized foams can be explained by the adsorbed HP-film at the air-water interface. Due to their special properties, HPs pack very tightly and form strong films at the air-water interface.[64] These films stabilize the air bubbles well in the liquid. As a result, they remain smaller.

HP-BSA Mixtures

Figure 7 shows the temporal evolution of the mean equivalent bubble diameter, mean circularity and dispersity of foams stabilized by mixtures of HP and BSA compared to systems stabilized by one of these proteins. Mixtures were investigated at different ratios: 3 wt% HP +1 wt% BSA, 2 wt% HP +2 wt% BSA, and 1 wt% HP +3 wt% BSA. The differences in between the foams stabilized by mixtures are distinctly less pronounced as compared to purely HP-stabilized foams.

HP forms monolayers with very regular patterns (rodlets) at the air-water interface.[45] As explained above, these highly amphipathic layers stabilize the foam well. Foam stability decreases significantly when BSA is added to HP foams: All foams stabilized by blends of HP and BSA show mean bubble diameters closer to those of BSA-stabilized foams than to those of HP-stabilized foams. Only at the end of the measurement period, the mean bubble diameter of foams stabilized by HP-BSA mixtures becomes distinguishably smaller than that of BSA-stabilized foams, but still remains significantly larger than that of HP-stabilized foams. Therefore, BSA seems to impede the regular arrangement of HP molecules at the interface. Consequently, the structures of the protein networks at the air-water interface are less regular and the emulsifying proteins are not able to achieve the same stability as in HP-stabilized foams.

The microscope images and the results of the analysis also show that the bubble shapes of foams stabilized by blends of HP and BSA are more similar to BSA-stabilized foams. The circularity of foams stabilized by HP-BSA blends is comparable to that of foams stabilized by BSA alone, while HP-stabilized foams show significantly higher circularity. For the dispersity, the trend is less pronounced. Mixtures of HP and BSA show dispersities in between those of BSA- and HP-stabilized foams with 2 wt% HP +2 wt% BSA showing a similar dispersity as 4 wt% HP.

These investigations show that differences in foam structure in relation to molecular differences can be well characterized by choosing the three parameters equivalent bubble diameter, circularity, and dispersity resulting from image analysis. This can be achieved using simple methods and freely available software. Therefore, the developed method can be used to study different systems and understand how they influence foam stability and structure.

Bubble Diameter Distribution

The dispersity of the equivalent bubble diameters offers a measure of the bubble size distribution. However, to investigate the bubble diameter distribution in more detail, histograms of the equivalent bubble diameters are shown in Figure 8. Each histogram includes the bubbles detected for three identically prepared samples. Additionally, in each plot the histograms of the bubble size distributions at the beginning, after 15 min and after 30 min are shown to investigate the temporal evolution. Over time, the bubble size distribution becomes broader in every investigated case. This trend can be explained by Ostwald-ripening. Over time, large bubbles grow and small

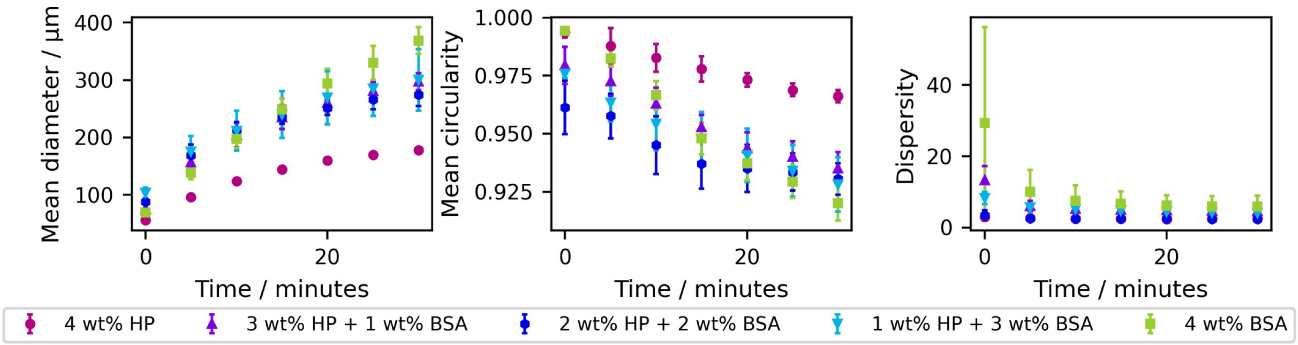

Figure 7. Comparison of the temporal evolution of mean equivalent bubble diameter, mean circularity and dispersity of HP- and BSA-stabilized foams, as well as differently concentrated mixtures of HP and BSA.

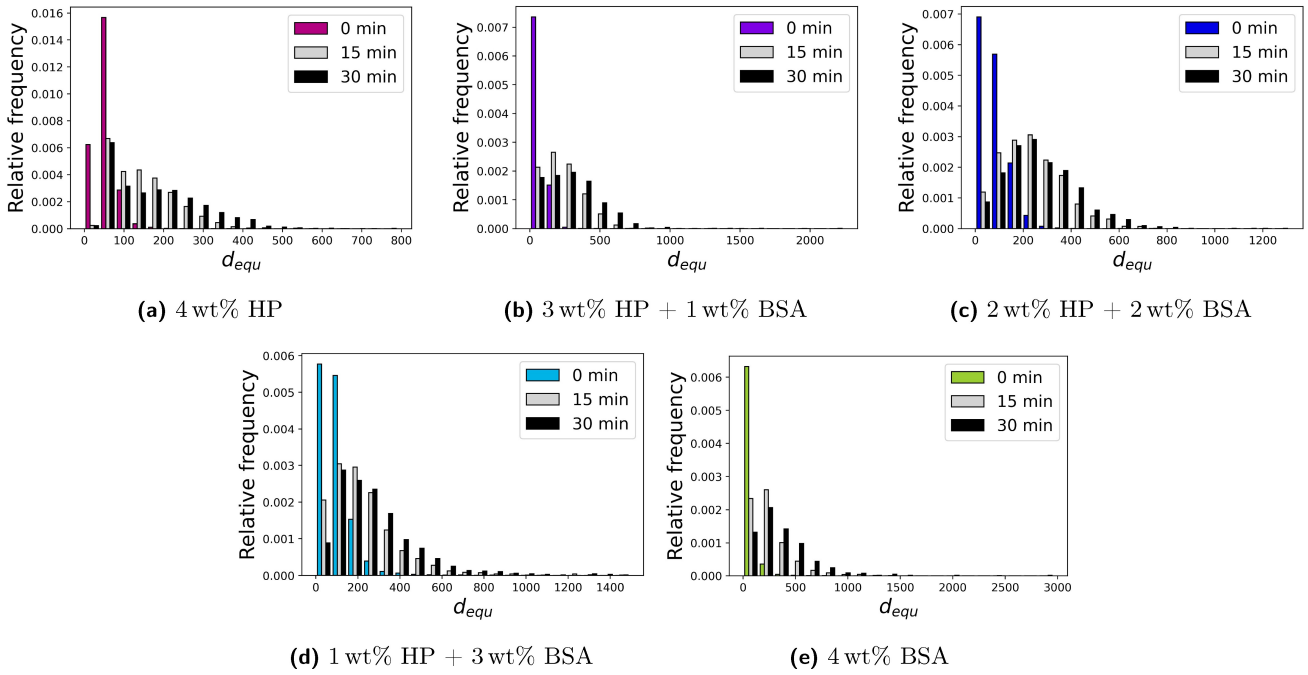

(a) 4 wt% HP **(b)** 3 wt% HP + 1 wt% BSA **(c)** 2 wt% HP + 2 wt% BSA

(d) 1 wt% HP + 3 wt% BSA **(e)** 4 wt% BSA

Figure 8. Temporal evolution of the equivalent bubble diameter distribution. Ostwald ripening leads to a broader size distribution in the course of time.

bubbles shrink due to the pressure differences between differently sized bubbles (Laplace pressure).[20,70,71] The growth of large bubbles at the expense of small bubbles leads to a broader bubble size distribution. The disappearance of tiny bubbles due to Ostwald ripening is further observed in the histograms and represents one of the most obvious temporal changes, especially at the beginning of the process. Therefore, the detection of tiny bubbles is important to study Ostwald ripening.

To compare the different proteins and their mixtures see Figure 9. With increasing BSA content, the size distribution becomes broader, which is in agreement with the higher dispersity and the presence of larger bubbles at the beginning of the measurements.

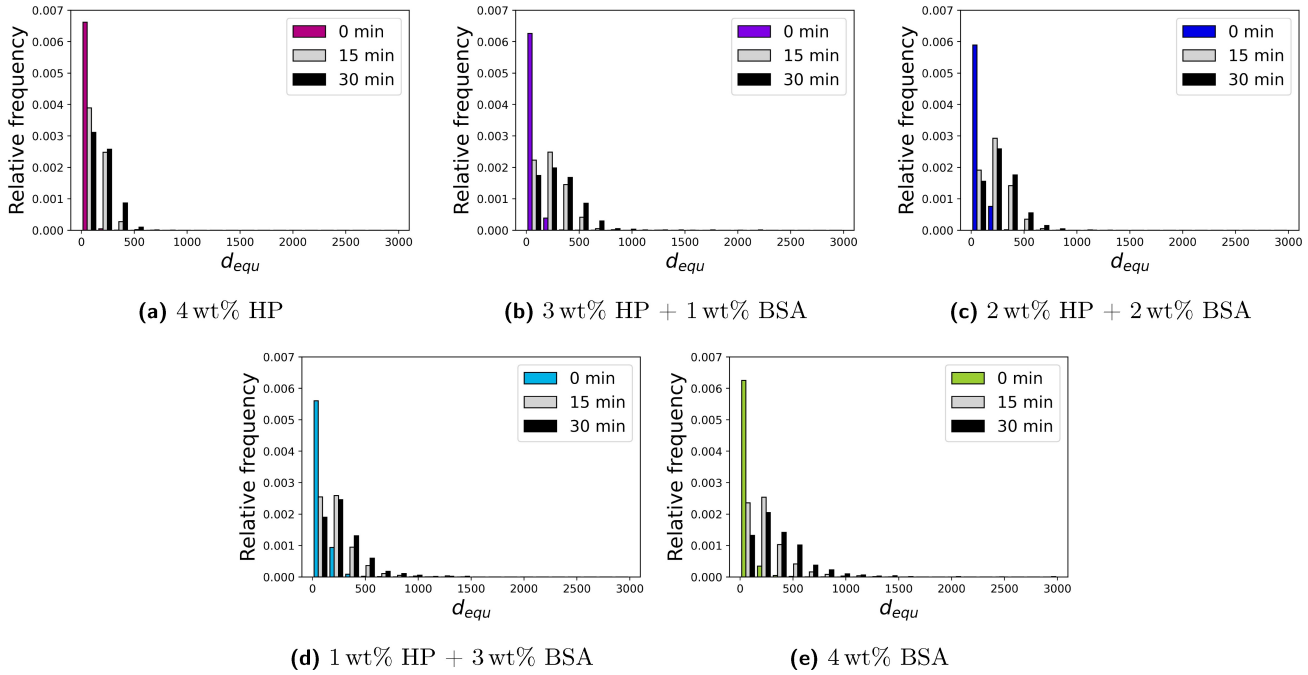

(a) 4 wt% HP **(b)** 3 wt% HP + 1 wt% BSA **(c)** 2 wt% HP + 2 wt% BSA

(d) 1 wt% HP + 3 wt% BSA **(e)** 4 wt% BSA

Figure 9. Temporal evolution of the equivalent bubble diameter distribution. Samples with a higher BSA content show a broader size distribution.

Economic Aspect

The employed software in the current method for automated analysis of the temporal evolution of foams is freely available and we provide the code for data analysis in the Supporting Information. Therefore, the costs for using the proposed method are lower than commercially available software.

Furthermore, the time investment is lower by using the proposed method than by using uncommercial analytical methods classically applied in fundamental research. A classical way of analyzing the sizes of bubbles in a foam is to measure the bubble size by hand.[12–14] The microscope images used in this study contain about 200 to 5000 bubbles each. Measuring 100 bubble diameters manually by drawing corresponding lines in *ImageJ* takes about 4 min to 10 min, which corresponds to about 2.5 s to 5 s per bubble. The needed time depends on the bubble size. To measure all bubble sizes in one image would then take between 17 min and 7 h depending on the number of bubbles contained in the image. Therefore, this method is very time intensive. Alternatively, one could only measure a few bubbles by hand to reduce the invested time. However, this approach biases the precision of the analyzed data.

The segmentation with *Cellpose* takes, depending on the number of bubbles, between 5 s and 60 s (about 70 s for two sets of masks) per image. Including the data analysis with our script, the total time of segmentation and analysis is about 2 min. Figure 10 shows a comparison of measuring the bubble diameters manually and analyzing the bubble properties with the presented approach. Manual measurement of the bubble diameter not only takes more time, but also does not provide information about the bubble shape.

Another approach is to threshold an image and determine the object sizes from the areas of connected same color pixels in the binary image. Figure 11 shows a section of a microscope

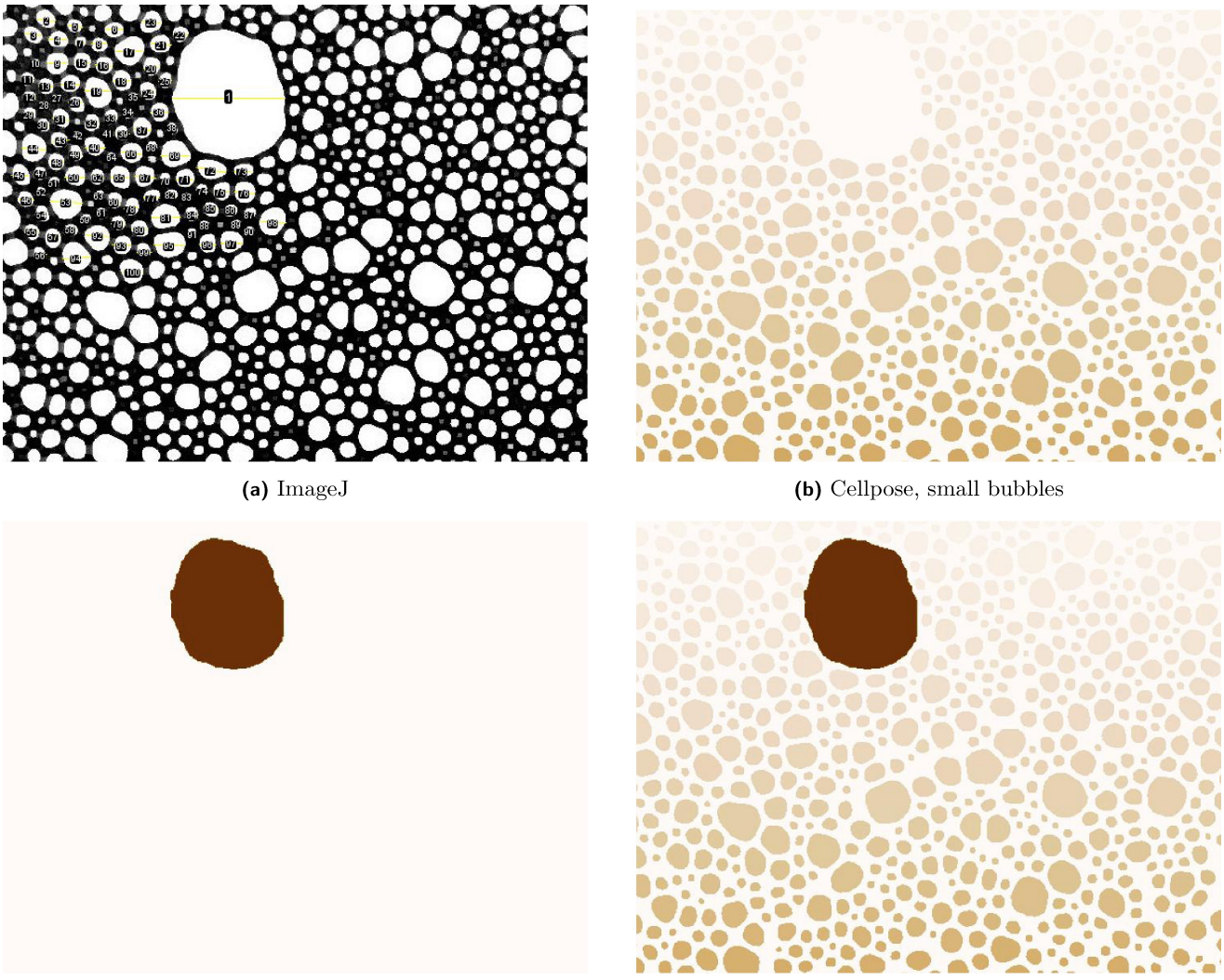

(a) ImageJ

(b) Cellpose, small bubbles

(c) Cellpose, large bubbles

(d) Small and large bubbles combined

Figure 10. (a) Microscope image of foam, where 100 bubble diameters where measured by hand using *ImageJ*.[72] The required time was 4 min 26 s. (b) Segmentation of small bubbles performed with *Cellpose* on the same microscope image. The required time was 57 s. (c) Segmentation of large bubbles. The required time was 5 s. (d) Addition of small and large bubble masks. The required time for adding the masks and analyzing the bubble properties was 35 s. Therefore, in total 1 min 37 s were required to analyze the image with the proposed method. For better visability, cutouts of the images are shown. To see the whole image, refer to Subfigure 5i.

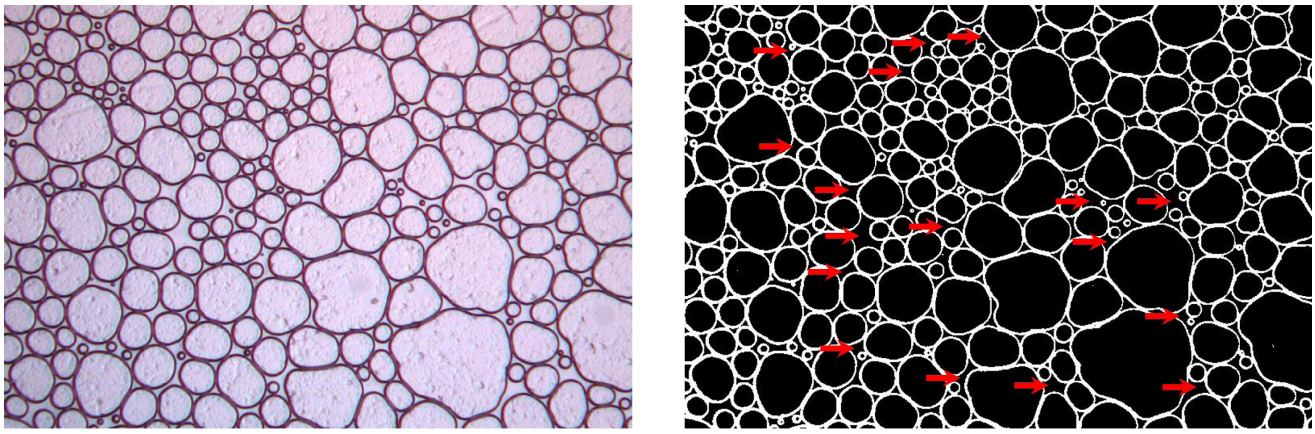

(a) Microscope image **(b)** Thresholded image

Figure 11. (a) Microscope image and (b) thresholded image of a HP foam. The red arrows mark example areas of continuous phase, which cannot be distinguished from bubble interior by contrast alone.

image of a HP foam and the same image where a threshold was applied using *ImageJ*.[72] Since the interior of the bubble and of the continuous phase have the same gray level, the difference cannot be extracted using a threshold. Therefore, thresholding is not sufficient for detecting objects in these kinds of samples. For this reason, the use of a machine learning algorithm and/or the possibility for manual correction leads to higher precision in detecting the bubbles correctly.

Furthermore, the *Cellpose* GUI offers the possibility to manually correct bubble masks to improve the precision. To what extend this option is used, is up to the user.

With the addition of two (or more) sets of masks for tiny bubbles and larger bubbles, our suggested method provides a greatly improved precision.

Conclusions

The developed method proves to be a useful and relevant tool for quantitative analysis of microscope images. It allows automated analysis of the temporal evolution of foams, including bubble growth, size distribution and bubble shape. Variations caused by different emulsifiers can be detected and analyzed quantitatively and economically, offering great advantages over expensive setups commonly used to determine bubble stability. The investigations show that the data analysis is consistent with visual observation. The large number of bubbles detected in each image provides significant statistics to ensure the reproducibility of the calculated quantities.

The example analysis of HP- and BSA-stabilized foams shows that the choice of emulsifier influences the foam structure and stability. Bubble size and shape vary depending on the properties of the emulsifier. The two proteins selected have different molecular structures. HP has a large hydrophobic patch on its surface and assembles into very strong films with regular patterns at the air-water interface.[44,45,64] These properties result in a significantly more stable foam and a rounder bubble shape. By analyzing microscope images with the presented method, it is demonstrated how mixing the two proteins influences their arrangement and the resulting stability.

Thus, using simple laboratory equipment and open source software, we are able to introduce our developed method as a way to analyze foams and draw meaningful conclusions.

Author Contributions

Judith Krom: Formal analysis, Investigation, Methodology, Project administration, Software, Visualization, Writing – original draft; Konrad Meister: Resources, Supervision; Thomas A. Vilgis: Resources, Supervision, Writing – review & editing.

Acknowledgements

The German Research Foundation is acknowledged for financial support to K.M. via DFG grant (ME 5344/1-1). K.M. acknowledges support through the BUILD Dairy network. Open Access funding enabled and organized by Projekt DEAL.

Conflicts of interest

There are no conflicts to declare.

Data Availability Statement

The data that support the findings of this study are available from the corresponding author upon reasonable request.

Keywords: foam · image analysis · stability · hydrophobin · protein · BSA

[1] K. Engelhardt, A. Rumpel, J. Walter, J. Dombrowski, U. Kulozik, B. Braunschweig, W. Peukert, *Langmuir* **2012**, *28*, 7780.
[2] X. Chen, Y. Chen, L. Zou, X. Zhang, Y. Dong, J. Tang, D. J. McClements, W. Liu, *J. Agric. Food Chem.* **2019**, *67*, 6574.
[3] K. G. Marinova, E. S. Basheva, B. Nenova, M. Temelska, A. Y. Mirarefi, B. Campbell, I. B. Ivanov, *Food Hydrocolloids* **2009**, *23*, 1864.
[4] Y. Yu, H. Zhang, J. Zhu, J. Liu, T. Zhang, *J. Food Sci.* **2020**, *85*, 4312.
[5] M. Zhao, W. Xiong, B. Chen, J. Zhu, L. Wang, *Food Hydrocolloids* **2020**, *103*, 105626.
[6] Z. Zhu, X. Mao, Q. Wu, J. Zhang, X. Deng, *J. Food Sci.* **2021**, *86*, 824.
[7] E. Zielińska, M. Karaś, B. Baraniak, *LWT-Food Sci. Technol.* **2018**, *91*, 168.
[8] K. Oetjen, C. Bilke-Krause, M. Madani, T. Willers, *Colloids Surf. A* **2014**, *460*, 280.
[9] M. Brüls, S. Foroutanparsa, T. Merland, C. E. P. Maljaars, M. M. Olsthoorn, R. P. Tas, I. K. Voets, *Food Struct.* **2023**, *38*, 100352.
[10] L. L. Olijve, A. S. Oude Vrielink, I. K. Voets, *Cryst. Growth Des.* **2016**, *16*, 4190.
[11] M. Pachitariu, C. Stringer, *Nat. Methods* **2022**, *19*, 1634.
[12] J. Schindelin, I. Arganda-Carreras, E. Frise, V. Kaynig, M. Longair, T. Pietzsch, S. Preibisch, C. Rueden, S. Saalfeld, B. Schmid, J.-Y. Tinevez, D. J. White, V. Hartenstein, K. Eliceiri, P. Tomancak, A. Cardona, *Nat. Methods* **2012**, *9*, 676.
[13] J. Saad, M. Fomich, V. P. Día, T. Wang, *Cryobiology* **2023**, *111*, 1.
[14] D. K. Sarker, D. Bertrand, Y. Chtioui, Y. Popineau, *J. Texture Stud.* **1998**, *29*, 15.
[15] L. Nichele, V. Persichetti, M. Lucidi, G. Cincotti, *OSA Continuum* **2020**, *3*, 1417.
[16] S. M. Hartig, *Curr. Protoc. Molec. Bio.* **2013**, *102*, 14.15.1.
[17] J.-C. Isarin, A. D. Kaasjager, R. B. Holweg, *Text. Res. J.* **1995**, *65*, 61.
[18] S. P. Gido, D. E. Hirt, S. M. Montgomery, R. K. Prud'homme, L. Rebenfeld, *J. Dispersion Sci. Technol.* **1989**, *10*, 785.
[19] C. Stringer, T. Wang, M. Michaelos, M. Pachitariu, *Nat. Methods* **2021**, *18*, 100.
[20] S. Damodaran, *J. Food Sci.* **2005**, *70*, R54.
[21] J. M. Rodríguez Patino, C. Carrera Sánchez, M. R. Rodríguez Niño, *Adv. Colloid Interface Sci.* **2008**, *140*, 95.
[22] N. J. Apthorpe, A. J. Riordan, R. E. Aguilar, J. Homann, Y. Gu, D. W. Tank, H. S. Seung, *Adv. Neural Inform. Processing Syst.* **2016**, *29*.
[23] F. A. Guerrero-Pena, P. D. Marrero Fernandez, T. I. Ren, M. Yui, E. Rothenberg, A. Cunha, Multiclass weighted loss for instance segmentation of cluttered cells, in *2018 25th IEEE International Conference on Image Processing (ICIP)*, IEEE **2018**, pages 2451–2455.
[24] Y. Al-Kofahi, A. Zaltsman, R. Graves, W. Marshall, M. Rusu, *BMC Bioinf.* **2018**, *19*, 1.
[25] J. Chen, L. Ding, M. P. Viana, H. Lee, M. F. Sluezwski, B. Morris, M. C. Hendershott, R. Yang, I. A. Mueller, S. M. Rafelski, *BioRxiv* **2020**.
[26] J. Funke, L. Mais, A. Champion, N. Dye, D. Kainmueller, A benchmark for epithelial cell tracking, in *Proceedings of The European Conference on Computer Vision (ECCV) Workshops*, Computer Vision Foundation, **2018**, pages 1–9.
[27] J. Yi, H. Tang, P. Wu, B. Liu, D. J. Hoeppner, D. N. Metaxas, L. Han, W. Fan, Object-guided instance segmentation for biological images, in *Proceedings of the AAAI Conference on Artificial Intelligence*, vol. 34, **2020**, pages 12677–12684.
[28] M. Aggarwal, A. K. Tiwari, M. P. Sarathi, A. Bijalwan, *BMC Med. Inf. Decis. Making* **2023**, *23*, 1.
[29] L. Ahmed, M. M. Iqbal, H. Aldabbas, S. Khalid, Y. Saleem, S. Saeed, *J. Ambient Intell. Human. Comput.* **2023**, *14*, 15227.
[30] X. Liu, L. Song, S. Liu, Y. Zhang, *Sustainability* **2021**, *13*, 1224.
[31] C. McQuin, A. Goodman, V. Chernyshev, L. Kamentsky, B. A. Cimini, K. W. Karhohs, M. Doan, L. Ding, S. M. Rafelski, D. Thirstrup, et al., *PLoS Biol.* **2018**, *16*, e2005970.
[32] J. C. Bonilla, J. L. Sørensen, A. S. Warming, M. P. Clausen, *Food Hydrocolloids* **2022**, *133*, 108010.
[33] S. Tcholakova, Z. Mitrinova, K. Golemanov, N. D. Denkov, M. Vethamuthu, K. P. Ananthapadmanabhan, *Langmuir* **2011**, *27*, 14807.
[34] D. Langevin, *Curr. Opin. Colloid Interface Sci.* **2019**, *44*, 23, 10.1016/j.cocis.2019.09.001, Memorial Volume.
[35] D.-M. Smilgies, E. Folta-Stogniew, *J. Appl. Crystallogr.* **2015**, *48*, 1604.
[36] E. Mylonas, D. I. Svergun, *J. Appl. Crystallogr.* **2007**, *40*, s245.
[37] S. Akiyama, *J. Appl. Crystallogr.* **2010**, *43*, 237.
[38] S. Bienert, A. Waterhouse, T. A. P. de Beer, G. Tauriello, G. Studer, L. Bordoli, T. Schwede, *Nucleic Acids Res.* **2017**, *45*, D313.
[39] The UniProt Consortium, *Nucleic Acids Res.* **2022**, *51*, D523, uniProtKB: P02769.
[40] R. T. Duarte, M. C. Carvalho Simões, V. C. Sgarbieri, *J. Agric. Food Chem.* **1999**, *47*, 231.
[41] Z. Litwińczuk, J. Król, A. Brodziak, J. Barłowska, *J. Dairy Sci.* **2011**, *94*, 684.
[42] M. B. Linder, G. R. Szilvay, T. Nakari-Setälä, M. E. Penttilä, *FEMS Microbiol. Rev.* **2005**, *29*, 877.
[43] H. A. Wösten, *Annual Reviews in Microbiology* **2001**, *55*, 625.
[44] S. Perrett, A. K. Buell, T. P. Knowles, *Biological and Bio-inspired Nanomaterials*, Springer **2019**.
[45] M. B. Linder, *Curr. Opin. Colloid Interface Sci.* **2009**, *14*, 356.
[46] J. G. Wessels, *Adv. Microb. Physiol.* **1997**, *38*, 1.
[47] H. A. Wösten, M.-A. van Wetter, L. G. Lugones, H. C. van der Mei, H. J. Busscher, J. G. Wessels, *Curr. Biol.* **1999**, *9*, 85.
[48] B. von Vacano, R. Xu, S. Hirth, I. Herzenstiel, M. Rückel, T. Subkowski, U. Baus, *Anal. Bioanal. Chem.* **2011**, *400*, 2031.
[49] M. Sunde, A. H. Kwan, M. D. Templeton, R. E. Beever, J. P. Mackay, *Micron* **2008**, *39*, 773.
[50] N. D. Sallada, K. J. Dunn, B. W. Berger, *Biochemistry* **2018**, *57*, 645.
[51] A. R. Cox, F. Cagnol, A. B. Russell, M. J. Izzard, *Langmuir* **2007**, *23*, 7995.
[52] J. Hakanpää, A. Paananen, S. Askolin, T. Nakari-Setälä, T. Parkkinen, M. Penttilä, M. B. Linder, J. Rouvinen, *J. Biol. Chem.* **2004**, *279*, 534.
[53] Q. Ren, A. H. Kwan, M. Sunde, *Proteins Struct. Funct. Bioinf.* **2014**, *82*, 990.
[54] C. L. Pham, A. Rey, V. Lo, M. Soulès, Q. Ren, G. Meisl, T. P. Knowles, A. H. Kwan, M. Sunde, *Sci. Rep.* **2016**, *6*, 25288.
[55] S. Askolin, M. Linder, K. Scholtmeijer, M. Tenkanen, M. Penttilä, M. L. de Vocht, H. A. Wösten, *Biomacromolecules* **2006**, *7*, 1295.
[56] W. Van der Vegt, H. Van der Mei, H. Wösten, J. Wessels, H. Busscher, *Biophys. Chem.* **1996**, *57*, 253.
[57] R. D. Stanimirova, T. D. Gurkov, P. A. Kralchevsky, K. T. Balashev, S. D. Stoyanov, E. G. Pelan, *Langmuir* **2013**, *29*, 6053.
[58] A. R. Cox, D. L. Aldred, A. B. Russell, *Food Hydrocolloids* **2009**, *23*, 366.
[59] T. Blijdenstein, P. De Groot, S. Stoyanov, *Soft Matter* **2010**, *6*, 1799.
[60] G. Fang, B. Tang, Z. Liu, J. Gou, Y. Zhang, H. Xu, X. Tang, *Eur. J. Pharm. Sci.* **2014**, *60*, 1.
[61] R. D. Waniska, J. E. Kinsella, *J. Food Sci.* **1979**, *44*, 1398.
[62] R. Gilbert, M. Hess, A. Jenkins, R. Jones, P. Kratochvil, R. Stepto, *Pure Appl. Chem.* **2009**, *81*, 351.
[63] S. Koltzenburg, M. Maskos, O. Nuyken, *Polymer chemistry*, Springer **2017**.
[64] B. S. Murray, *Curr. Opin. Colloid Interface Sci.* **2007**, *12*, 232.
[65] O. Pitois, Foam Ripening, in *Foam Engineering: Fundamentals and Applications*, John Wiley & Sons **2012**, pages 59–73.
[66] S. González-Pérez, J. M. Vereijken, G. A. van Koningsveld, H. Gruppen, A. G. Voragen, *J. Agric. Food Chem.* **2005**, *53*, 6469.
[67] W. Drenckhan, S. Hutzler, *Adv. Colloid Interface Sci.* **2015**, *224*, 1.
[68] S. Omirbekov, H. Davarzani, S. Colombano, A. Ahmadi-Senichault, *Adv. Water Resour.* **2020**, *146*, 103761.
[69] L. L. Schramm, F. Wassmuth, Foams: basic principles, in *Foams: Fundamentals and Applications in the Petroleum Industry*, chapter 1, pages 3–45, *ACS Publications* **1994**.
[70] R. J. Pugh, *Bubble and Foam Chemistry*, Cambridge University Press **2016**.
[71] I. Cantat, S. Cohen-Addad, F. Elias, F. Graner, R. Höhler, O. Pitois, F. Rouyer, A. Saint-Jalmes, *Foams: Structure and Dynamics*, Oxford University Press **2013**.
[72] C. A. Schneider, W. S. Rasband, K. W. Eliceiri, *Nat. Methods* **2012**, *9*, 671.

Manuscript received: January 18, 2024
Revised manuscript received: April 25, 2024
Accepted manuscript online: April 29, 2024
Version of record online: July 1, 2024